Direct numerical simulations of liquid films in two dimensions under horizontal and vertical external vibrations

Sebastian Richter* and Michael Bestehorn
Department of Theoretical Physics, Statistical Physics and Nonlinear Dynamics, Brandenburg University of Technology, Cottbus, Germany

(Received 4 October 2018; published 16 April 2019)

We consider Newtonian liquid films on a horizontal substrate with a free and deformable surface. The substrate is subjected to oscillatory accelerations in the normal or in the horizontal direction. An algorithm based on a nonlinear coordinate transformation is presented that allows for direct numerical solutions of the fully nonlinear Navier-Stokes equations and appropriate boundary conditions. No surface tracking is necessary. Normal oscillations generate the traditional subharmonic and harmonic Faraday patterns. Lateral oscillations cause a pattern formation scenario qualitatively similar to spinodal dewetting, namely the disintegration of the film into isolated drops followed by coarsening or fusion, the stabilization of a "precursor" film, and no rupture. Ratchet-like lateral excitations break the horizontal mirror symmetry $x \to -x$ and give the patterns a preferred direction. We show that drops formed due to instability of the flat film start to travel in a distinguished direction. For thin films, the results are in good agreement to those of a recently studied lubrication-based dimension-reduced model [Bestehorn *et al.*, Phys. Rev. E **88**, 023025 (2013); Bestehorn, Phys. Fluids **25**, 114106 (2013)].

DOI: 10.1103/PhysRevFluids.4.044004

I. INTRODUCTION

The first pattern-forming instability in fluids was discovered experimentally by Michael Faraday in 1831 [1]. A vertically vibrating liquid with an originally flat free surface may show regular surface deformations that normally have the form of regular squares. The squares oscillate with half of the driver's frequency and are in resonance with gravity waves of the unforced liquid. More than 120 years after Faraday's experiments, a first simplified theoretical treatment of the linearized hydrodynamic basic equations assuming an inviscid fluid was given by Benjamin and Ursell [2]. The stability problem of the fluid in rest can be reduced to a Mathieu equation. Later, the analysis was extended to viscous fluids [3,4] for layers with arbitrary depth. This work was experimentally confirmed in Ref. [5]. Instabilities and pattern formation were studied in experiments, for example [6], showing beneath the original subharmonic structures also harmonic branches where the patterns oscillate with the same frequency as the driver. Vertical oscillations can also be used to suppress the Rayleigh-Taylor instability where a heavier fluid is positioned over a lighter ones, as was shown in early experiments by Wolf [7] for small aspect ratios and later numerically in Ref. [8] for a two-layer thin film setup.

In large aspect ratios the patterns are normally rather regular and may emerge as the classical squares, but also stripes, hexagons [9], or even quasicrystals with eightfold [10] or twelvefold symmetries [11,12] can be encountered.

*Corresponding author: richtseb@b-tu.de

Although Faraday already considered oscillations of the layer tangential to the free flat surface, most of the work up to now deals with normal (classical) excitation. The first theoretical paper that studied in-plane oscillations (further referred to as "horizontal") was by Yih in 1968 [13]. Yih showed that the flat surface becomes unstable with respect to a long wave instability, in contrast to the normal excitation, where a disturbance with a finite critical wave number branches off the base state at onset.

Experiments on horizontal excitations are still rare. A series of experiments for thicker layers with depth of the size of the wavelength have been performed by Porter *et al.* [14–17]. The problem here is the lateral walls which prevent the existence of a horizontally homogeneous base flow and which when oscillating laterally act as wave makers. In experiments, a laterally (one-dimensional) periodic container could be approximated by taking an annular ring cell with large radius, as developed earlier for convection experiments (see, e.g., [18,19]). In other experiments, Yoshikawa and Wesfreid [20] considered a horizontally excited two-layer system and interpreted the observed patterns as Kelvin-Helmholtz instability [21]. The spatio-temporal dynamics of a diffusive interface between miscible liquids also under microgravity conditions was extensively studied by Gaponenko *et al.* [22,23]. Theoretical work by Lyubimov and Cherepanov [24] predicted the formation of spatially stationary interfacial instabilities ("frozen waves") between two immiscible fluids subjected to horizontal vibration, a result which was later proved in experimental investigations by Ivanova *et al.* [25]. Lyubimova theoretically studied the influence of horizontal vibrations on Marangoni instability [26]. Experiments and a stability analysis by Talib *et al.* [27,28] revealed the role of viscosity contrast.

Based on lubrication theory, dimension-reduced models can be derived systematically by integrating out the vertical dimension; see, e.g., [29]. In this way inertia terms of the original Navier-Stokes equations can be kept approximately, as further developed by Ruyer-Quil and Manneville [30] and later by Rojas *et al.* [31].

In Refs. [32,33] a dimension-reduced model was systematically derived that allows for the examination of nonlinear pattern formation for the normal, the horizontal, and the combined cases of oscillations. The model fully includes inertia, an important ingredient for parametric instabilities. The free deformable surface is considered in the way of the thin film (Reynolds lubrication) equation—see, e.g., [34]—and no interface tracking is necessary. This model was applied further to two-layer systems [8,35] and to three-dimensional (3D) one-layer systems to demonstrate the existence of quasiperiodic spatial structures [36]. The linearized reduced model can be directly compared to the linearized Navier-Stokes equations, as was done in Refs. [32,33].

To show the validity of the model in the nonlinear regime, numerical solutions of the fully nonlinear basic equations are desirable. Up to now, only very few papers have dealt with numerical solutions of the full Navier-Stokes equations for the standard Faraday instability, most of them in 2D [37–39]. To our knowledge there is no numerical work on horizontal or combined excitations.

The present paper has two main purposes: (i) to devise a numerical scheme for the fully nonlinear system without further approximations, and (ii) to justify the nonlinear computations performed with the reduced model in Refs. [32,33]. For the case of horizontal excitations, we confirm the occurrence of traveling localized surface elevations if the time dependence of the lateral excitation $f_x(t)$ has the form of a ratchet, so that $f_x(t) \neq -f_x(t+t_0)$ for arbitrary t_0. These traveling drops were predicted earlier by our model and are now computed using the full Navier-Stokes equations.

The paper is organized as follows: In the next two sections the algorithm is described starting from the 2D hydrodynamic basic equations and boundary conditions. The key idea is the mapping of the deformed area to a rectangle $[L \times 1]$, applying the nonlinear transformation $x = \tilde{x},\ z = h(x,t)\,\tilde{z}$, where $h(x,t)$ describes the position of the free surface, $x, \tilde{x}$ run from zero to L and $\tilde{z}$ from zero to one. This transformation was first used in Ref. [40] to examine the formation and the dynamics of bores in an inviscid fluid.

Section III shows the numerical discretization and implementation on a staggered grid. The pressure is computed exactly from the incompressibility condition at each time step by solving a sparse linear system obtained from the transformed Poisson equation.

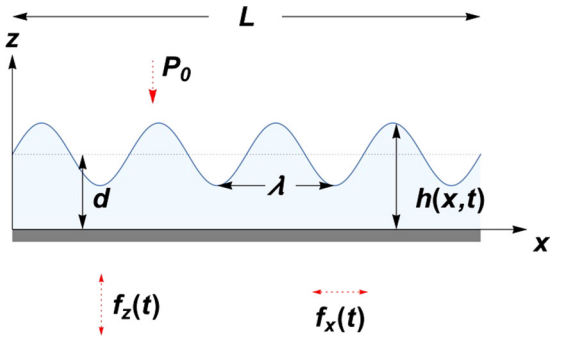

FIG. 1. Incompressible Newtonian fluid on a plane substrate with mean depth d and with a free surface at $z = h(x, t)$. The liquid is subjected to a time-dependent force field or the substrate is vibrating in vertical $[f_z(t)]$ and horizontal $[f_x(t)]$ directions. Due to periodic excitation with a sufficiently large amplitude value, instability of the flat film occurs and surface structures with wavelength λ appear.

Section IV presents numerical results for normal and horizontal excitations. Both cases are compared with the outcome of the reduced model [32,33] and a good agreement is found. Finally, asymmetric ratchet-like horizontal forcing that breaks the $x \to -x$ symmetry is applied, showing traveling localized surface elevations to the left or to the right, depending on the form of the excitation.

II. BASIC EQUATIONS

A. Navier-Stokes equations

We consider an incompressible fluid layer described by the two-dimensional Navier-Stokes equations. The layer is bounded in vertical direction by a planar horizontal substrate at $z = 0$ and by its free surface at $z = h(x, t)$ (Fig. 1). Periodic boundary conditions are assumed in the lateral direction. The sum of external forces acting on the system is given by

$$\vec{f}(t) = \begin{pmatrix} f_x(t) \\ f_z(t) \end{pmatrix} = g \begin{pmatrix} a_x(t) \\ a_z(t) - 1 \end{pmatrix}, \tag{1}$$

where g is the constant gravitational acceleration and ga_i denotes a time-periodic acceleration

$$a_i(t) = a_i(t + T). \tag{2}$$

Using the viscosity ν, density ρ, and the mean depth d we can apply the scalings

$$\vec{x} = d\,\tilde{\vec{x}}, \quad t = (d^2/\nu)\,\tilde{t}, \quad h = d\,\tilde{h}, \tag{3a}$$

$$\vec{v} = (\nu/d)\,\tilde{\vec{v}}, \quad P = (\nu^2\rho/d^2)\,\tilde{P}, \quad \gamma = (\nu^2\rho/d)\,\Gamma, \quad \vec{f} = (\nu^2/d^3)\,\tilde{\vec{f}} \tag{3b}$$

of length $\vec{x} = (x, z)$, time t, layer depth h, velocity field $\vec{v} = (v, w)$, pressure P, and surface tension γ in order to receive the following dimensionless notation (henceforth, we drop the tildes):

$$\frac{\partial \vec{v}}{\partial t} + (\vec{v} \cdot \nabla)\vec{v} + \nabla P - \Delta \vec{v} - \vec{f}(t) = 0, \tag{4a}$$

$$\nabla \cdot \vec{v} = 0. \tag{4b}$$

With (4b), Poisson's equation

$$\Delta P = 2(\partial_x u \partial_z w - \partial_x w \partial_z u) \tag{5}$$

determining the pressure field inside the fluid is obtained, forming the divergence of Eq. (4a).

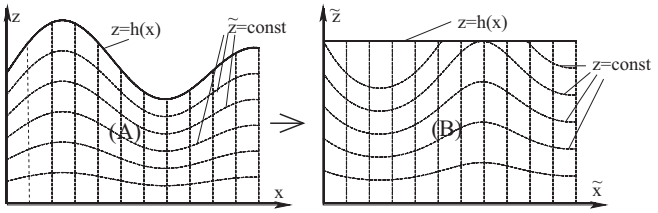

FIG. 2. Nonlinear coordinate transformation (13) of a fluid layer (A) with arbitrarily shaped surface to a rectangle (B).

B. Boundary conditions

The toroidal domain geometry (periodic lateral boundary conditions) implies

$$\vec{v}(x,z,t) = \vec{v}(x+L,z,t), \quad h(x,t) = h(x+L,t) \tag{6}$$

with L being the scaled horizontal length of the layer. At the bottom ($z = 0$), the velocity field vanishes according to the no-slip condition:

$$\vec{v}(x,z=0,t) = 0. \tag{7}$$

The force equilibrium at the free surface can be formulated as the relation (tangential shearing forces disappear)

$$\hat{\vec{t}} \cdot \sigma|_{z=h} \cdot \hat{\vec{n}} = 0 \tag{8}$$

between unit tangent vector $\hat{\vec{t}}$, unit normal vector $\hat{\vec{n}}$, and scaled deviatoric stress tensor σ:

$$\hat{\vec{t}} = \frac{1}{\sqrt{1+h'^2}}\begin{pmatrix}1\\ h'\end{pmatrix}, \quad \hat{\vec{n}} = \frac{1}{\sqrt{1+h'^2}}\begin{pmatrix}-h'\\ 1\end{pmatrix}. \tag{9}$$

Furthermore, vanishing normal stress components deliver the condition

$$(\sigma \cdot \hat{\vec{n}})_{z=h} = (P_0 - P_{z=h} - \Gamma\mathcal{K})\,\hat{\vec{n}}. \tag{10}$$

Here, P_0 is the constant atmospheric pressure, Γ denotes the inverse capillary number (scaled surface tension), and the curvature of the free surface is described by

$$\mathcal{K} = \frac{h''}{(1+h'^2)^{3/2}}, \tag{11}$$

where the first and the second derivatives with respect to x are abbreviated as h' and h'', respectively. The kinematic boundary condition

$$\frac{\partial h}{\partial t} = \left(w - u\frac{\partial h}{\partial x}\right)_{z=h} \tag{12}$$

completes the set of equations.

C. Mapping

In Ref. [40], we introduced the local nonlinear coordinate transformation

$$x = \tilde{x}, \quad z = h(x,t)\cdot\tilde{z} \tag{13}$$

which will pare the required interpolation of the later numerical scheme down to a minimum. The mapping transforms an arbitrarily shaped, time-dependent fluid layer to a rectangular region (Fig. 2).

Thus, the identities and conditions (4), (8), (10), and (12) must be converted according to (13). The transformed first-order derivatives read

$$\frac{\partial}{\partial x} = \frac{\partial}{\partial \tilde{x}} - \tilde{z}\frac{h'}{h}\frac{\partial}{\partial \tilde{z}}, \quad \frac{\partial}{\partial z} = \frac{1}{h}\frac{\partial}{\partial \tilde{z}}, \quad \frac{\partial}{\partial t} = \frac{\partial}{\partial \tilde{t}} - \tilde{z}\frac{\dot{h}}{h}\frac{\partial}{\partial \tilde{z}}. \tag{14}$$

For the second-order derivatives we find

$$\frac{\partial^2}{\partial x^2} = \frac{\partial^2}{\partial \tilde{x}^2} + \tilde{z}\left(2\left(\frac{h'}{h}\right)^2 - \frac{h''}{h}\right)\frac{\partial}{\partial \tilde{z}} - 2\tilde{z}\frac{h'}{h}\frac{\partial^2}{\partial \tilde{x}\,\partial \tilde{z}} + \tilde{z}^2\left(\frac{h'}{h}\right)^2\frac{\partial^2}{\partial \tilde{z}^2}, \tag{15a}$$

$$\frac{\partial^2}{\partial z^2} = \frac{1}{h^2}\frac{\partial^2}{\partial \tilde{z}^2}. \tag{15b}$$

Inserting (14) and (15) into the Navier-Stokes equation and the mass conservation equation yields (we drop all tildes again)

$$\frac{\partial u}{\partial t} = z\dot{\xi}\frac{\partial u}{\partial z} - u\left(\frac{\partial u}{\partial x} - z\xi'\frac{\partial u}{\partial z}\right) - \frac{w}{h}\frac{\partial u}{\partial z} - \frac{\partial P}{\partial x} + z\xi'\frac{\partial P}{\partial z} + \Delta u + f_x(t), \tag{16a}$$

$$\frac{\partial w}{\partial t} = z\dot{\xi}\frac{\partial w}{\partial z} - u\left(\frac{\partial w}{\partial x} - z\xi'\frac{\partial w}{\partial z}\right) - \frac{w}{h}\frac{\partial w}{\partial z} - \frac{1}{h}\frac{\partial P}{\partial z} + \Delta w + f_z(t), \tag{16b}$$

and

$$\frac{\partial u}{\partial x} - z\xi'\frac{\partial u}{\partial z} + \frac{1}{h}\frac{\partial w}{\partial z} = 0, \tag{17}$$

respectively, where the auxiliary variable

$$\xi(x,t) = \ln h(x,t) \tag{18}$$

is introduced for the sake of convenience. Laplace's operator in Eqs. (16) changes into

$$\Delta = \frac{\partial^2}{\partial x^2} + \frac{(zh')^2 + 1}{h^2}\frac{\partial^2}{\partial z^2} + \frac{z}{h}\left(\frac{2}{h}h'^2 - h''\right)\frac{\partial}{\partial z} - \frac{2zh'}{h}\frac{\partial^2}{\partial x\,\partial z}.$$

The transformation maps the horizontal and, in case of $z = 0$, the vertical coordinate to themselves. Hence, this does not affect the lateral boundary condition (6) or the no-slip condition (7). Equation (8) has to be rewritten though, considering (13), and solved for $u|_{z=h}$ to calculate the lateral components of the velocity at the surface. The continuity equation (17) is used to eliminate $\partial_z w$ in Eq. (8). After transforming the stress tensor we may rearrange Eq. (8) to

$$\partial_z u|_{z=1} = \frac{h}{(1+h'^2)^2}\left(h'(h'^2+3)\frac{\partial u}{\partial x} - (1-h'^2)\frac{\partial w}{\partial x}\right). \tag{19}$$

From the projection of Eq. (10) on the normal vector, we receive the condition

$$P|_{z=1} = -\Gamma\mathcal{K} - \frac{2}{1+h'^2}\left(\frac{\partial u}{\partial x} + h'\frac{\partial w}{\partial x}\right)_{z=1} \tag{20}$$

for the pressure at $z = 1$, where the pressure is normalized to $P_0 = 0$. The boundary condition for P at the liquid-substrate interface ($z = 0$) can be derived by evaluating the z component of (16b) with $\vec{v} = 0$:

$$\left(\frac{\partial P}{\partial z}\right)_{z=0} = \frac{1}{h}\left(\frac{\partial^2 w}{\partial z^2}\right)_{z=0} + h f_z(t). \tag{21}$$

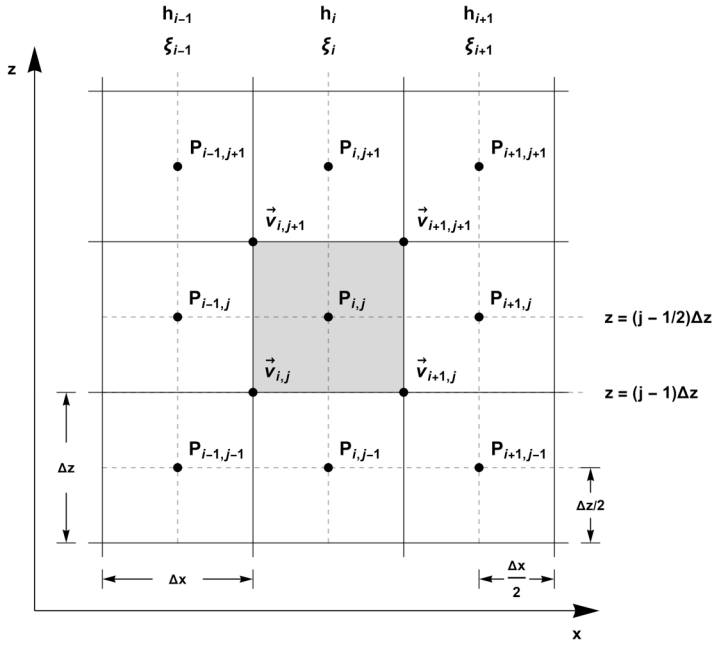

FIG. 3. Staggered grid consisting of two uniform grids shifted with respect to each other by $\Delta x/2$ and $\Delta z/2$ in the x and z directions, respectively.

III. THE ALGORITHM

A. Implementation

The rectangular domain is discretized by an equidistant, two-dimensional Cartesian grid $D = [x_1, x_2, \ldots, x_M] \times [z_1, z_2, \ldots, z_N]$ with M and N mesh points in x (horizontal) and z (vertical) directions, respectively. Thus, the step sizes read

$$\Delta x = \frac{L}{M}, \quad \Delta z = \frac{1}{N-1}, \tag{22}$$

where L is given in units of d and the spacial discretizations are

$$x_i = (i-1)\Delta x, \quad z_j = (j-1)\Delta z. \tag{23}$$

The time is uniformly quantized:

$$t_n = n\Delta t. \tag{24}$$

We are using the notations

$$A_{ij} = A_{ij}^{(n)} = A(x_i, z_j, t_n), \quad A_i = A_i^{(n)} = A(x_i, t_n) \tag{25}$$

for physical quantities at the point (x_i, z_j) or at the surface location (x_i).

B. Staggered grid

The velocities (u, w) are stored at the edges of each cell (v-grid), whereas the scalar quantities (P, h, and ξ) as well as their spatial and time derivatives are defined at the center positions (p-grid) (Fig. 3). Variables discretized on the p-grid can be converted to the v-grid, and vice versa, applying linear interpolation. We use the half-index notation

$$A_{i,j\pm1/2} = \tfrac{1}{2}(A_{ij} + A_{i,j\pm1}), \quad A_{i\pm1/2,j} = \tfrac{1}{2}(A_{ij} + A_{i\pm1,j}), \quad A_{i\pm1/2} = \tfrac{1}{2}(A_i + A_{i\pm1}) \tag{26}$$

to calculate variables at intermediate positions.

C. Time update

The temporal evolution of the system is obtained by calculating the transitions

$$h(x,t) \to h(x,t+\Delta t),$$
$$\vec{v}(x,z,t) \to \vec{v}(x,z,t+\Delta t), \tag{27}$$

for each grid point (x,z). The new height at the time step $n+1$ ensues from the kinematic boundary condition (12). It is beneficial to use the conservative form

$$\dot{h} = -\frac{\partial q(x,t)}{\partial x}, \tag{28}$$

where

$$q(x,t) = h(x,t)\int_0^1 dz\, u(x,z,t) \tag{29}$$

is the mass flux, since (28) conserves the mass globally. The discretized form of (28) reads

$$h_i^{(n+1)} = h_i - \Delta t\,\Delta z \frac{\sum_{j=1}^N u_{i+1,j}h_{i+1/2} - \sum_{j=1}^N u_{ij}h_{i-1/2}}{\Delta x}. \tag{30}$$

The new velocities are found from the discretized form of the Navier-Stokes equations (16) according to

$$\frac{u_{ij}^{(n+1)}}{\Delta t} = F_{ij}^x - \frac{P_{i,j-1/2} - P_{i-1,j-1/2}}{\Delta x} + (j-1)\xi_{i-1/2}(P_{i-1/2,j} - P_{i-1/2,j-1}) + f_x(t), \tag{31a}$$

$$\frac{w_{ij}^{(n+1)}}{\Delta t} = F_{ij}^z - \frac{1}{h_{i-1/2}}\frac{P_{i-1/2,j} - P_{i-1/2,j-1}}{\Delta z} + f_z(t), \tag{31b}$$

where F^x, F^z stand for the discretized form of all terms of the Navier-Stokes equations except the derivatives of P, the external forces, and the velocity at the new time step. The detailed form of $\vec{F}$ is given in the Appendix.

D. Pressure

Before computing $\vec{v}$ with (31), the pressure has to be determined in such a way that the new velocities fulfill the continuity equation. If we insert (31) into the discretized continuity equation (17) on the p-grid,

$$0 = \frac{u_{i+1,j+1/2}^{(n+1)} - u_{i,j+1/2}^{(n+1)}}{\Delta x} - (j-1/2)\frac{\xi_{i+1}-\xi_{i-1}}{2\Delta x}\left(u_{i+1/2,j+2}^{(n+1)} - u_{i+1/2,j}^{(n+1)}\right) + \frac{1}{h_i}\frac{w_{i+1/2,j+1}^{(n+1)} - w_{i+1/2,j}^{(n+1)}}{\Delta z}, \tag{32}$$

we find an implicit relation for the pressure in the form of a sparse system of inhomogeneous equations:

$$\begin{aligned} &a_{ij}^1 P_{i-1,j-1} + a_{ij}^2 P_{i-1,j} + a_{ij}^3 P_{i-1,j+1} + a_{ij}^4 P_{i,j-1} + a_{ij}^5 P_{i,j} + a_{ij}^6 P_{i,j+1} + a_{ij}^7 P_{i+1,j-1} \\ &+ a_{ij}^8 P_{i+1,j} + a_{ij}^9 P_{i+1,j+1} = -\frac{F_{i+1,j+1}^x + F_{i+1,j}^x - F_{i,j+1}^x - F_{i,j}^x}{2\Delta x} \\ &+ \left(j - \frac{1}{2}\right)\frac{\xi_{i+1}-\xi_{i-1}}{4\Delta x}\left(F_{i+1,j+1}^x + F_{i,j+1}^x - F_{i+1,j}^x - F_{i,j}^x\right) \\ &- \frac{1}{h_i}\frac{F_{i+1,j+1}^z + F_{i,j+1}^z - F_{i+1,j}^z - F_{i,j}^z}{2\Delta z}, \end{aligned} \tag{33}$$

where the nine coefficients a_{ij}^k are listed in the Appendix. The right-hand side of the system is the divergence of the vector $\vec{F} = (F^x, F^z)$. Since j runs from 1 to $N-1$, one has to take the boundary conditions for P into account. Equations (21) and (20) yield

$$P_{i,0} = P_{i,1} + \Delta z\left(f_z h_i - \frac{w_{i+1,2} + w_{i,2}}{h_i \Delta z^2}\right) \tag{34}$$

and

$$\begin{aligned} P_{i,N} = &-\frac{\Gamma(h_{i+1} + h_{i-1} - 2h_i)}{\Delta x^2\left(1 + \left(\frac{h_{i+1}-h_{i-1}}{2\Delta x}\right)^2\right)^{3/2}} - \frac{u_{i+1,N+1} + u_{i+1,N} - u_{i,N+1} - u_{i,N}}{\Delta x\left(1 + \left(\frac{h_{i+1}-h_{i-1}}{2\Delta x}\right)^2\right)} \\ &- \frac{(h_{i+1} - h_{i-1})(w_{i+1,N+1} + w_{i+1,N} - w_{i,N+1} - w_{i,N})}{2\Delta x\left(1 + \left(\frac{h_{i+1}-h_{i-1}}{2\Delta x}\right)^2\right)} \end{aligned} \tag{35}$$

respectively. We consult condition (19) to find the discretization of the lateral velocity field at the surface, which is needed in Eq. (35) (along with the vertical component):

$$u_{i,N+1} = u_{i,N-1} + \frac{2\Delta z h_{i-1/2}}{1 + h_i'^2}\left(h_i'\left(h_i'^2 + 3\right)\frac{\partial u_{i,N}}{\partial x} - \left(1 - h_i'^2\right)\frac{\partial w_{i,N}}{\partial x}\right). \tag{36}$$

$w_{i,N+1}$ is received from (17):

$$w_{i,N+1} = w_{i,N-1} + 2\Delta z\left(h_i'\frac{\partial u_{i,N}}{\partial z} - h_{i-1/2}\frac{\partial u_{i,N}}{\partial x}\right). \tag{37}$$

The system (33) is sparse and can be solved for the pressure effectively by applying standard sparse schemes; see, e.g., [41].

E. Algorithm

We briefly summarize the main steps of the numerical procedure:

(1) Choose an initial state $\vec{v}_{ij} = \vec{v}(t=0)$, $h_i = h(t=0) > 0$, $\sum_i h_i = 1$ considering the continuity equation (17). Due to the nature of the nonlinear transformation presented in Sec. II C, relatively smooth fluid surfaces are strongly preferable. Noncompliance of this implicit condition may lead to nonvanishing chessboard patterns.

(2) Calculate $h_i^{(n+1)}$ from Eq. (30).

(3) Compute the pressure at each grid point by solving the sparse linear system (33)–(35).

(4) Calculate the velocities $u_{ij}^{(n+1)}$, $v_{ij}^{(n+1)}$ from (31).

(5) Set $t := t + \Delta t$, $h_i = h_i^{(n+1)}$, $u_{ij} = u_{ij}^{(n+1)}$, and $w_{ij} = w_{ij}^{(n+1)}$.

(6) Continue with item 2.

IV. RESULTS

A. Dimension-reduced lubrication model

In this section we wish to compare the results of our numerical simulations with a lubrication-approximation-based model first derived in Ref. [30] for a falling thin film and referred to there as a first-order model. It was extended in Ref. [32] to the case of external vibrations. Its linear stability as well as its nonlinear behavior were investigated in detail in Ref. [33]. Rojas *et al.* [31] showed the validity and truncation error of the model to be of the order of the Reynolds number.

Projecting the z dependence of the horizontal velocity onto a polynomial expansion, a separation of variables is achieved, permitting one to integrate out the vertical coordinate and thus reducing the

two spatial dimensions (x, z) to one (x). It reads

$$\frac{6}{5}\left[\partial_t q + \frac{9}{7}\partial_x\left(\frac{q^2}{h}\right) - \frac{1}{7}\frac{q\,\partial_x q}{h}\right] = -\frac{3}{h^2}\,q + h\partial_x[\Gamma\partial_{xx}h - \mathcal{G}(1 - a_z(t))h] + \mathcal{G}a_x(t)\,h, \quad (38a)$$

$$\partial_t h + \partial_x q = 0, \quad (38b)$$

where $q(x, t)$ is again the local mass flux as defined in Eq. (29) and $\mathcal{G} = gd^3/\nu^2$ is the Galilei number (for further details, see [33]).

B. Fluid parameters and initial conditions

To ensure the comparability to the Navier-Stokes equations we use the following general setup:

(1) For all simulations we take a silicone oil with the following material properties:

Density $\rho = 920\ \mathrm{kg/m^3}$, surface tension $\gamma = 0.02\ \mathrm{N/m}$, kinematic viscosity $\nu = 5 \times 10^{-6}\ \mathrm{m^2/s}$.

(2) The evolution of the fluid is investigated after the system has reached an energetic saturation which applies if the period-averaged total kinetic energy

$$\bar{E}_{\mathrm{kin}}(t) = (1/T)\int_{t-T}^{t} E_{\mathrm{kin}}(t')\,dt'$$

[with $E_{\mathrm{kin}}(t) \propto \int q^2\,dx$ and T given from (2)] remains approximately constant:

$$\forall t > t_e : \bar{E}_{\mathrm{kin}}(t_e) \approx \bar{E}_{\mathrm{kin}}(t).$$

For times greater than t_e the energy gain due to the external excitation is equal to the friction-induced energy transformation into heat.

(3) To demonstrate the independence on initial conditions we use the following cases:

(a) Point-symmetric initial conditions. The surface takes the form of a Gaussian function located at $x_0 = (i_0 - 1)\Delta x$, where the height of the peak δh is assumed to be small ($\delta h \ll 1$) and δx controls the width of the curve:

$$\forall (x_i, z_j) \in D : u(x_i, z_j, t_0) = w(x_i, z_j, t_0) = 0, \quad (39a)$$

$$h_i = \mathcal{N}\left[1 + \delta h\,\exp\left(-\left(\frac{\Delta x}{\delta x}(i - i_0)\right)^2\right)\right], \quad i = 1, \ldots, M, \quad (39b)$$

and $\mathcal{N}$ from the normalization $\sum_i h_i = 1$.

(b) Random initial conditions. A randomly shaped fluid surface (small variations to the mean depth at every point) is considered:

$$\forall (x_i, z_j) \in D : u(x_i, z_j, t_0) = w(x_i, z_j, t_0) = 0, \quad (40a)$$

$$\forall (x_i, z_j) \in D : h(x_i, z_j, t_0) = 1 + \delta h\,Z, \quad (40b)$$

where Z is an equally distributed random variable in $[-1/2, 1/2]$ with zero mean.

We measure the deviation of the emerging surface structures between both approaches quantitatively by introducing the distance function

$$\alpha^2(t) = \frac{1}{L}\int_0^L dx\,(h^{(1)}(x, t) - h^{(2)}(x, t))^2, \quad (41)$$

which takes the discretized form

$$\alpha^2(t) = \frac{1}{M}\sum_{i=1}^{M}\left(h_i^{(1)}(t) - h_i^{(2)}(t)\right)^2. \quad (42)$$

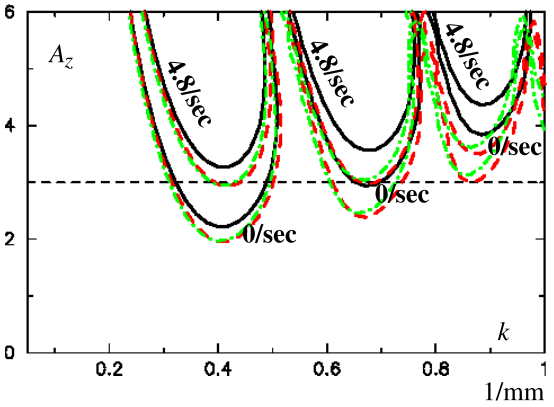

FIG. 4. Marginal growth rate $\lambda = 0$ and positive growth rate $\lambda = 4.8/\mathrm{s}$ for a silicone oil (see text) with depth $d = 0.7$ mm and $\omega_z/2\pi = 10$ Hz. The leftmost tongue becomes unstable first and the instability oscillates with half of the driver's frequency (subharmonic). The different lines correspond to the three cases: (i) solid (black), full Navier-Stokes; (ii) dashed dotted (green), lubrication approximation (iii) dashed (red), lubrication approximation with one Galerkin mode, model (38). Reproduced from [33], with the permission from AIP Publishing.

Here, $h^{(1)}$ is the layer depth calculated from the model (38) and $h^{(2)}$ is the depth gained from the present algorithm, Sec. III E (henceforth, the superscripts $^{(1)}$ and $^{(2)}$ are used with the same meaning).

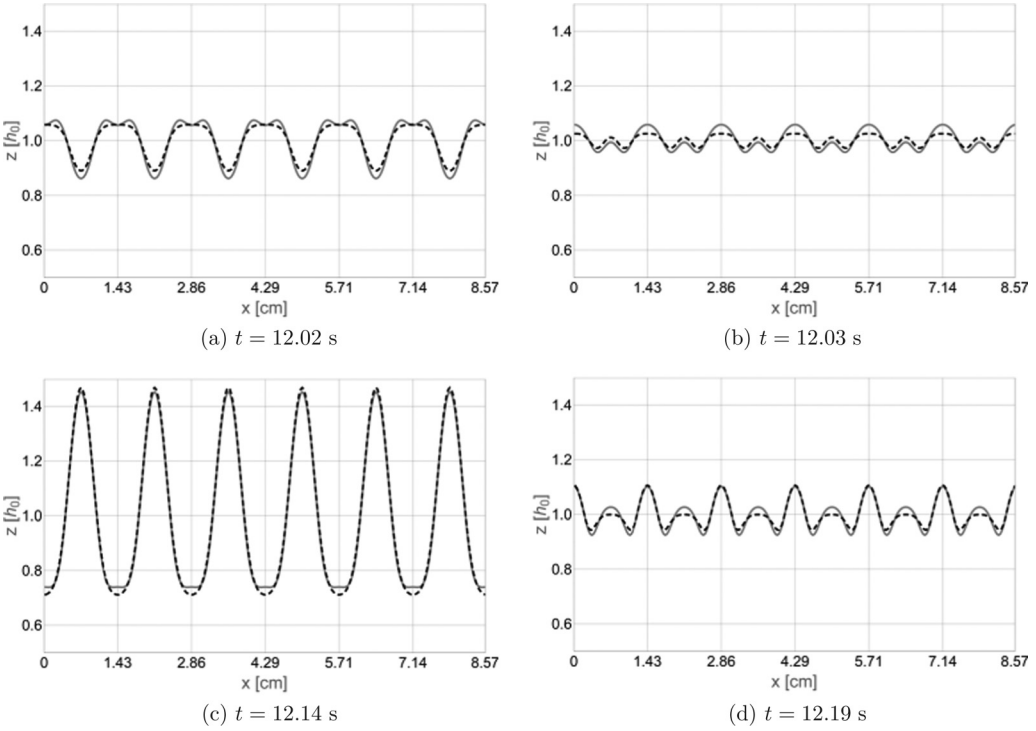

(a) $t = 12.02$ s (b) $t = 12.03$ s

(c) $t = 12.14$ s (d) $t = 12.19$ s

FIG. 5. Excited fluid layer with a domain length of 8.57 cm and mean depth 0.7 mm (numerical grid size is 300×20) after $t = 12$ s. Solid corresponds to the reduced model [see Eq. (38)] and the dashed line represents the system (33)–(37) (Navier-Stokes equations). The excitation frequency is $\omega_z/2\pi = 5$ Hz.

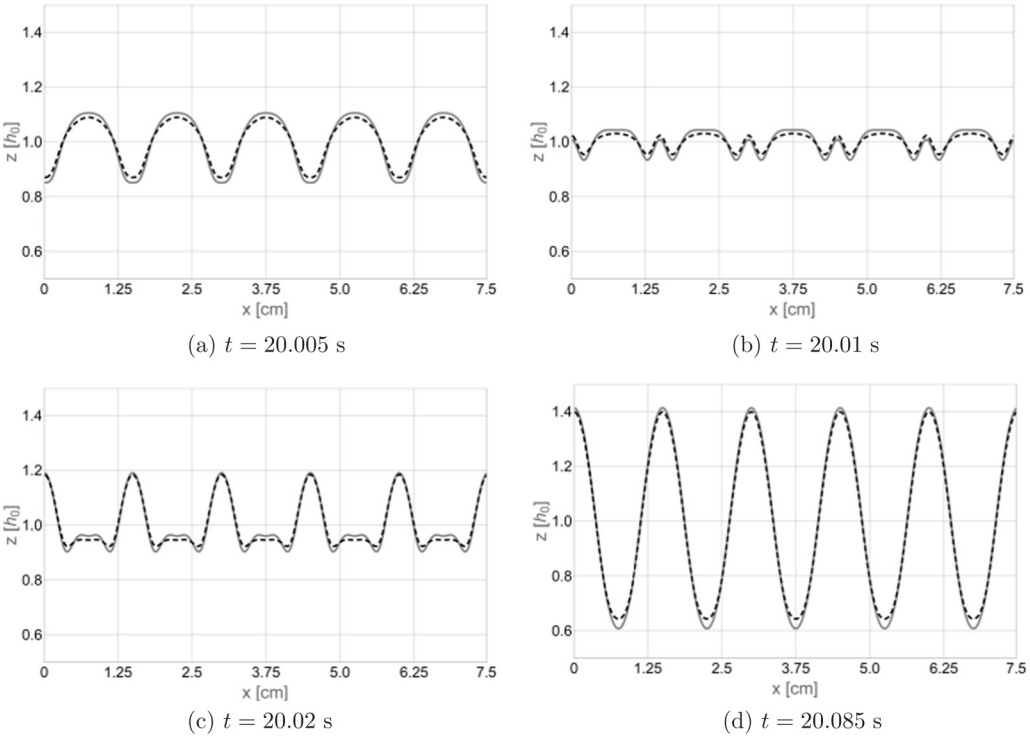

(a) $t = 20.005$ s (b) $t = 20.01$ s

(c) $t = 20.02$ s (d) $t = 20.085$ s

FIG. 6. Excited fluid layer with length 7.5 cm and mean depth 0.7 mm (numerical grid size is 300×20) after $t = 20$ s. The excitation frequency is $\omega_z/2\pi = 10$ Hz and the amplitudes are $A_z^{(1)} = 2.39$ and $A_z^{(2)} = 2.6$. Dashed: Navier-Stokes, solid: reduced model.

C. Harmonic excitation in the vertical direction

We start with a simple harmonic excitation $\vec{a}(t) = (0, A_z \cos(\omega_z t))$ in the z direction. The initial conditions do not affect the long-term evolution of the film. Up to an arbitrary lateral shift, both conditions (39) and (40) result in identical patterns for all cases investigated in this section.

A linear stability analysis performed in Refs. [32,33] showed that due to the lubrication approximation the Faraday tongues in the amplitude-wave number plane are shifted downwards, resulting in lower critical vibration amplitudes compared to those for the full linearized Navier-Stokes equations; see Fig. 4. As expected from the long-wave approximation, this discrepancy becomes more pronounced with decreasing wave length of the horizontal disturbances. For our parameters and a fluid depth of 0.7 mm, the difference of the first tongues is in the size of about 9%. To account for this fact, we use lower amplitudes of excitation for the lubrication model in order to adjust the maximum equilibrium heights after saturation:

$$\max_i h_i^{(1)} \stackrel{!}{=} \max_i h_i^{(2)}. \tag{43}$$

We examine harmonically and subharmonically oscillating liquids, making recourse to findings given in Ref. [33]. Instabilities that oscillate with the driver's frequency can be observed in low frequency ranges. At $\omega_z/2\pi = 5$ Hz, the critical amplitudes amount to $A_z^{(1)} \approx 2.7$ and $A_z^{(2)} \approx 2.9$ (ascertained by the linear stability analysis) and the critical wave numbers are approximately identical ($k_c^{(1)} \approx k_c^{(2)} \approx 0.44/\text{mm}$). The amplitudes are chosen above the stability threshold, allowing us to study the waves in the nonlinear regime. We take $A_z^{(1)} = 2.81$ and $A_z^{(2)} = 3.15$, values that fulfill the condition (43). The length of the layer is adjusted to integral multiples of the critical wavelength,

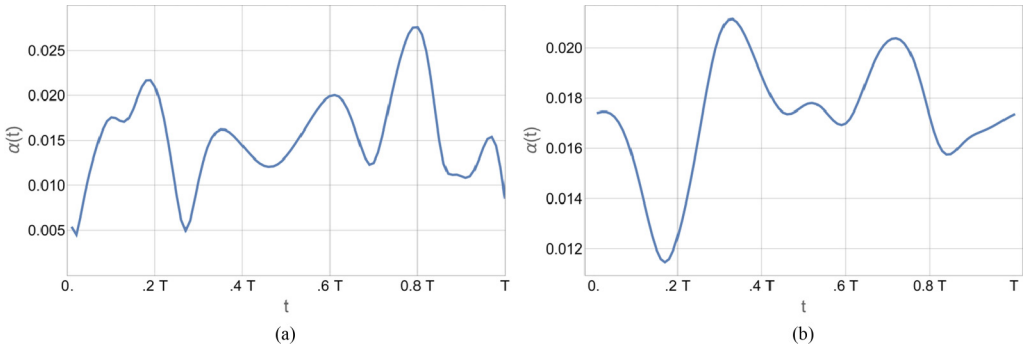

FIG. 7. Difference plot $\alpha(t)$ for one oscillation period T. Panels (a) and (b) correspond to the setups shown in Figs. 5 and 6.

here 6. Figure 5 shows the pattern formation for several times t within one period $T = 2\pi/\omega_z$. If we consider $\alpha(t)$ over time [Fig. 7(a)], we find good agreement between the models where the maximum difference is less then 3%.

Higher values of ω_z improve the agreement further. The fluid at the double frequency $\omega_z/2\pi = 10$ Hz oscillates subharmonically (Fig. 6) with half of the excitation frequency, and the difference reaches a value of only 2.2%; see Fig. 7(b). For the surface one finds the relation $h(x,t) = h(x + \lambda/2, t + T)$, showing the match between the generated patterns in the time intervals $[t,\ t+T]$ and $[t+T,\ t+2T]$. Both intervals produce the same surface structures, so we can omit the second half of the period in Fig. 7.

D. Harmonic excitation in horizontal direction

Next we consider the case $\vec{a}(t) = (A_x \cos(\omega_x t), 0)$ of a harmonic lateral force. The linear stability analysis is again taken from [33]; see Fig. 8.

Starting with random initial conditions (40), we track the evolution of the surface over time. Figure 9 shows the evolution of a rather thin layer with $d = 0.2$ mm until the minimal fluid depths approach the final values, which are about 0.02 mm. The linearly fastest growing wave number is $k_c \approx 0.5/\text{mm}$; see Fig. 8. After a first phase of exponential growth, the pattern becomes strongly

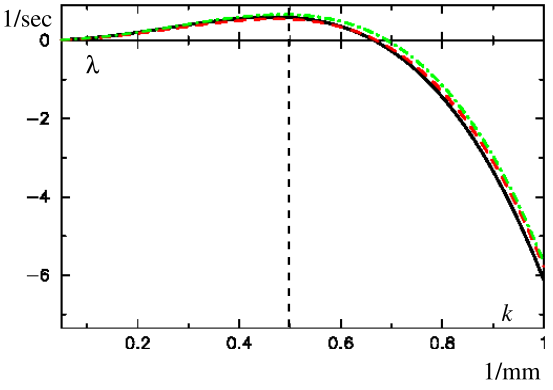

FIG. 8. Growth rate of long wave instability of a horizontally excited thin layer with $d = 0.2$ mm; for the meaning of the different lines see Fig. 4. The agreement between Navier-Stokes equations, lubrication approximation, and model is now much better. Dashed vertical line denotes k_c, the linearly fastest growing mode. Reproduced from [33], with the permission from AIP Publishing.

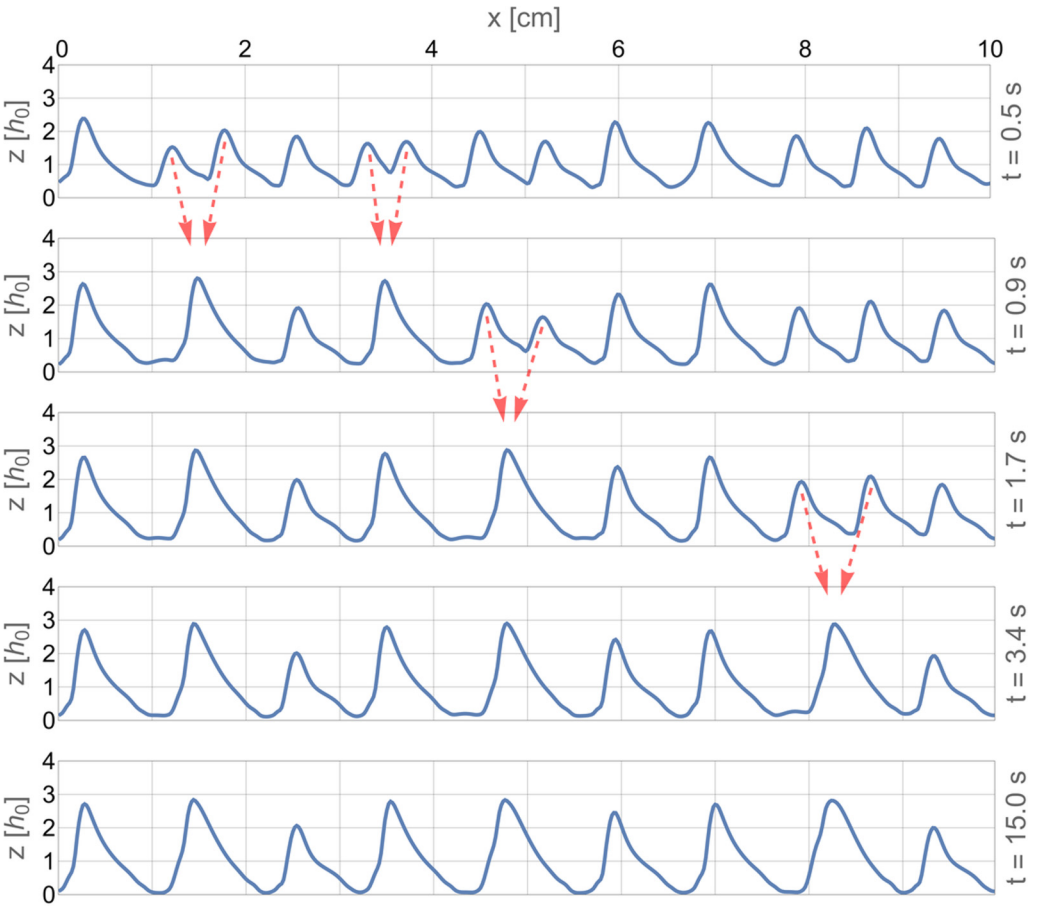

FIG. 9. Slow fusion process (arrows) with (45) and $\beta = 0$ computed from the Navier-Stokes equations with $\omega_x/2\pi = 40$ Hz and $A_x = 6.44$, for horizontal excitation. The average thickness is $d = 0.2$ mm, layer length $L = 0.1$ m, numerical grid size 500×10. No preferred direction of drop propagation can be seen.

nonlinear, the amplitudes saturate, and the liquid forms a number of separated droplets that start to merge very slowly. The domains between the drops stay completely covered with liquid, comparable to a rather thick "precursor-like" film, and rupture is not observed. After saturation, the number of remaining drops is approximately equal to the number of critical wavelengths that fit into the layer, and the merging process starts whereby the minimum thickness of the film remains almost constant. This findings are in good agreement with those of the model (38) from which the series depicted in Fig. 10 are computed for the same parameters and for the same geometry.

We find that the temporally asymptotic behavior is widely independent of the initial state and, as a consequence, point-symmetric conditions lead to qualitatively identical results for large times t.

E. Ratchet excitation in horizontal direction

Pattern dynamics is invariant under horizontal mirror symmetry $x \to -x,\ z \to z$ if the external force transforms as

$$a_x(t) \to -a_x(t + t_0), \quad a_z(t) \to a_z(t + t_0) \tag{44}$$

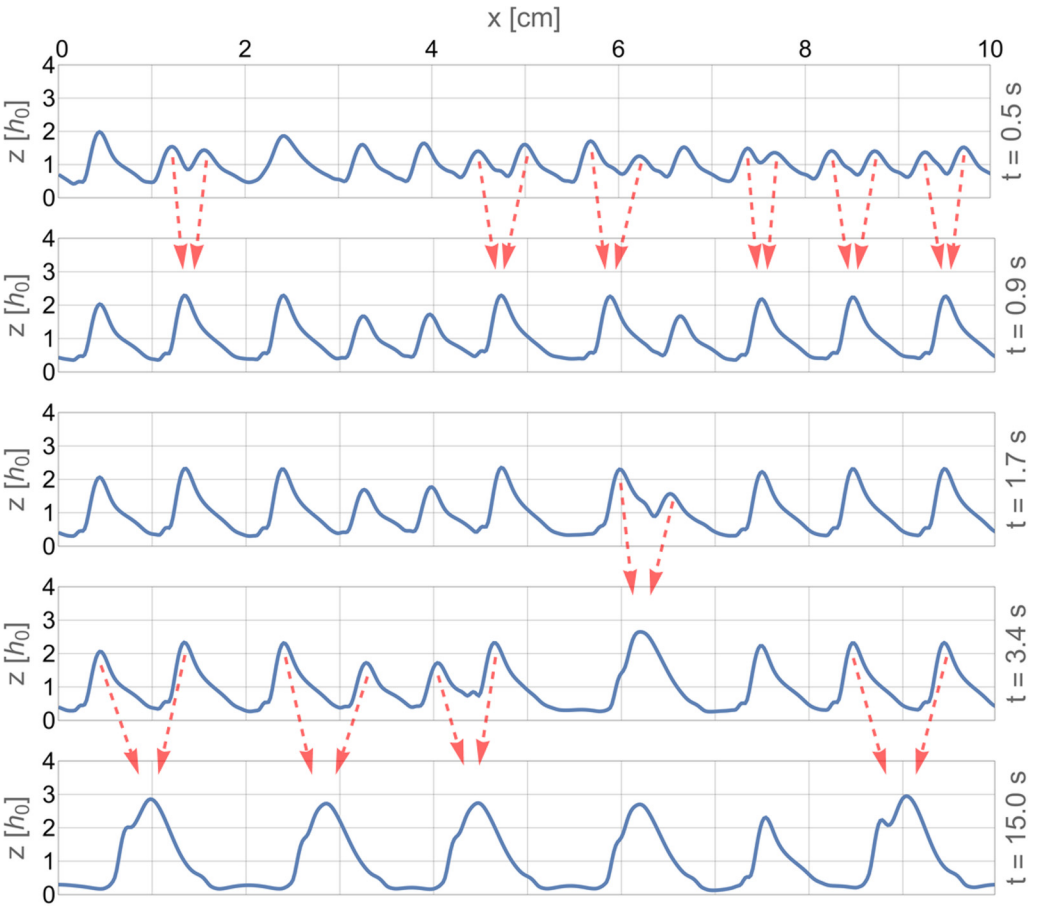

FIG. 10. Slow fusion process with (45) and $\beta = 0$ computed from the reduced model (38). Same parameters as in Fig. 9.

with a certain time offset t_0. Relations (44) of course hold for the forces examined in the preceding paragraphs, with $t_0 = 0$ for Sec. IV C and $t = \pi/\omega_x$ for Sec. IV D, and the observed patterns, stripes, or single isolated drops have no preferred direction of propagation. This changes in the moment when (44) cannot be fulfilled for any t_0, e.g., for an inclined oscillation of the substrate, according to $\vec{a}(t) = \vec{a}_0 \cos \omega t$ with $\vec{a}_0$ not normal *and* not parallel to the substrate. Another possibility, and this is the method we use in this paragraph, is a purely horizontal but time-reversal asymmetric external force $\vec{a}(t) = (a_x(t), 0)$, with

$$a_x = A_x[\sin(\omega_x t) + \beta \sin(2\omega_x t)]. \tag{45}$$

For $\beta < 0$, the substrate moves faster (and over shorter time) to the left side, followed by a slower (and longer) turn to the right, for $\beta > 0$ vice versa. The force (45) can be termed "ratchet excitation," and in fact the expression (45) reflects the first two terms of the Fourier expansion of a sawtooth. Drops similar to those obtained in Sec. IV D travel now due to the symmetry break $x \to -x$ in one preferred direction, namely to the left-hand side ($\beta < 0$), as was shown in Ref. [42] using the reduced model (38). An additional effect of the symmetry-breaking force is that the propagation speed of the drops depends on their size. This may accelerate the fusion process by orders of magnitude in time, since different-size drops may catch up each other and merge rapidly.

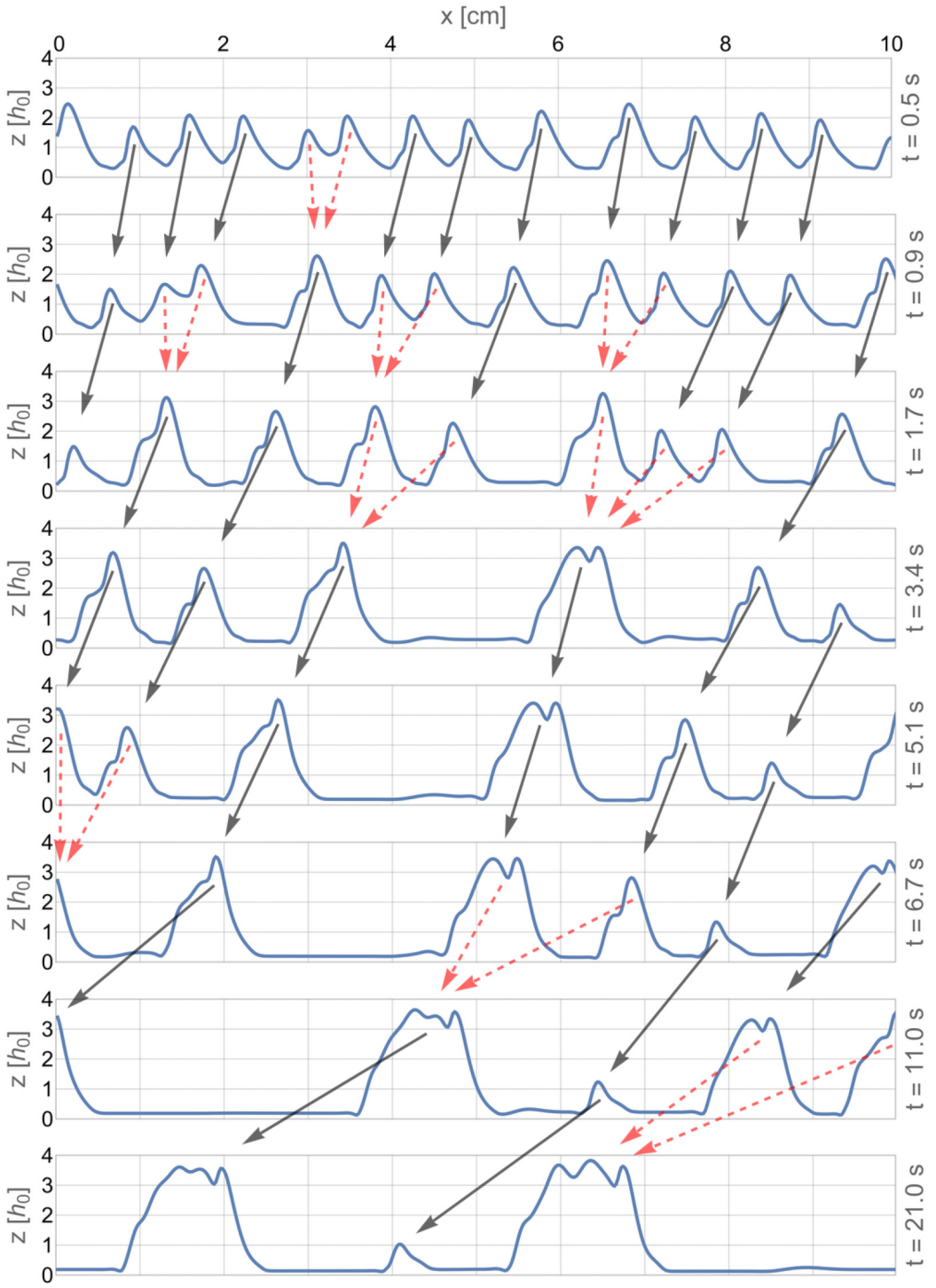

FIG. 11. Solution of the full Navier-Stokes equations. Fast fusion process (red dashed arrows) with (45) and $\beta = -1$; other parameters as in Fig. 9. Drops travel to the left-hand side (black solid arrows) and fusion is much faster in the nonlinear regime than in Fig. 9.

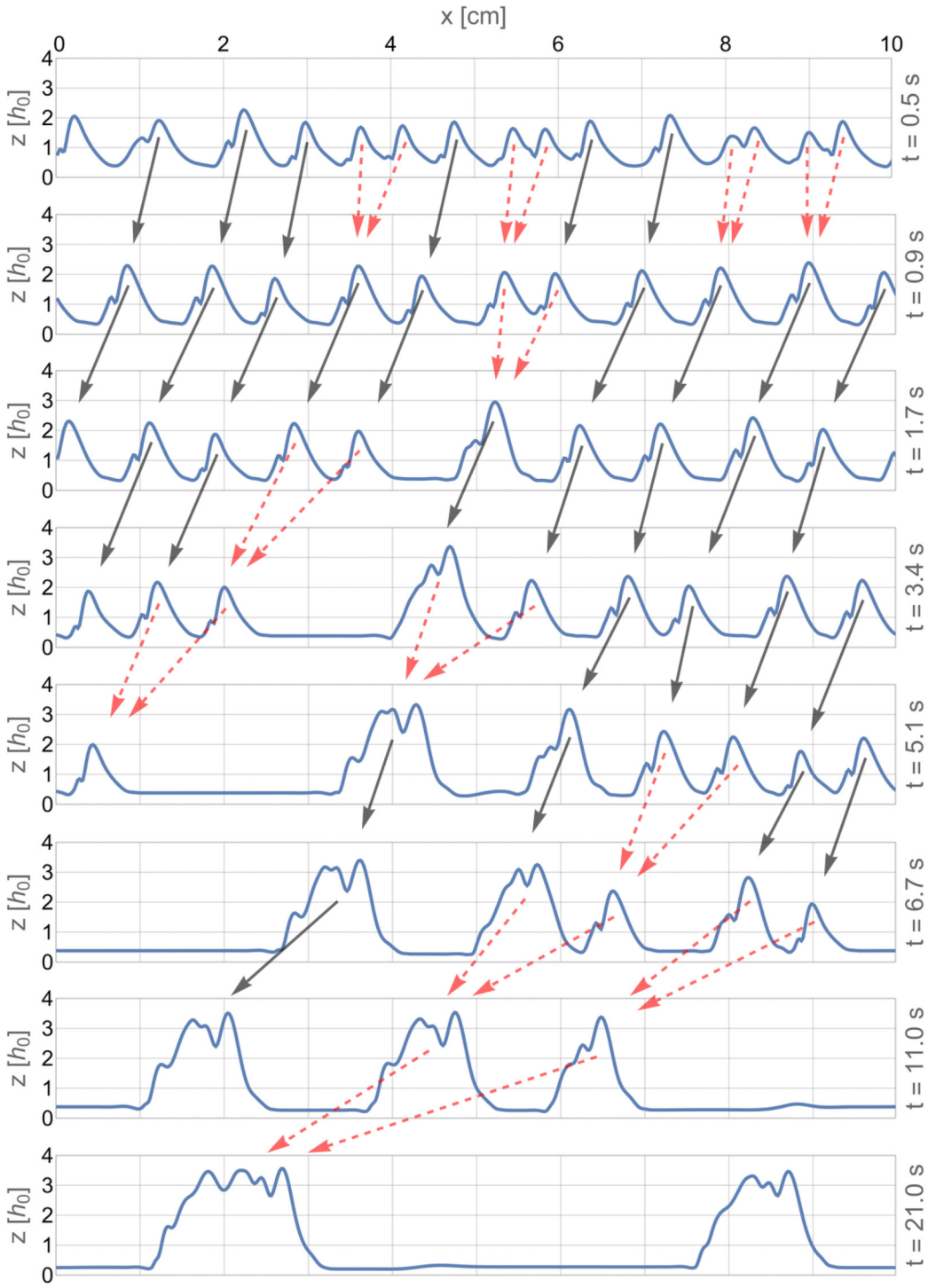

FIG. 12. Same as Fig. 11, but now as a result of the reduced model (38).

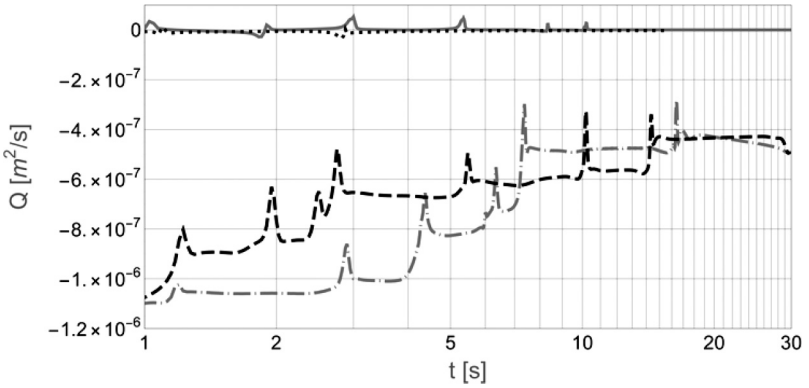

FIG. 13. Averaged mean flow $Q(t)$ according to (46). Dashed: Navier-Stokes with $\beta = -1$, dot-dashed: model with $\beta = -1$. Both series show constant plateaus interrupted by peaks when two drops merge; compare Figs. 11 and 12. Dotted (Navier-Stokes) and solid (model) lines are for $\beta = 0$ (Figs. 9 and 10), where Q is much smaller and significantly nonzero only when two drops merge into one.

The time series depicted in Figs. 11 and 12 again compare the outcome of the model (38) with the results of the full Navier-Stokes equations. The same features, namely main motion of the droplets to the left side and strong acceleration of fusion, can be obtained from both computations. For both initial conditions (39) and (40) we observe similar patterns, and the minimal thicknesses are about the same as those found in Sec. IV D.

As recently demonstrated in Ref. [42], the averaged mean flow

$$Q(t) = \frac{1}{LT} \int_{t-T}^{t} dt' \int_{0}^{L} dx\, q(x, t') \tag{46}$$

does not vanish for a symmetry-breaking lateral excitation given as (45). From Fig. 13 the temporal behavior of Q can be seen for the time series shown in Figs. 11 and 12. Q is nonzero from the time when drops are formed due to instability. It remains fairly constant until the moment when the first fusion takes place. Then it suffers a short decrease in its absolute value and reaches a smaller value after fusion, due to the fact that the structure resulting from two fused drops moves slower than the two separated drops before fusion. This behavior repeats until all drops are merged into one, which is still traveling, but slowly.

V. CONCLUSIONS

In this work we have studied pattern formation of laterally and vertically excited thin fluid films considering a finite-difference method for the solution of the Navier-Stokes equations. The asymptotic patterns developed by normally oscillating systems largely coincide with those calculated earlier from a simplified lubrication-approximation-based model. Classic harmonic and subharmonic Faraday waves can be observed in low and high frequency ranges, respectively.

We find that the results for laterally excited liquids are also in qualitative agreement with the reduced model. Identical stages of evolution exist (exponential growth, droplet formation, and fusion); the geometry of the formed drops and intermediate fluid layers differs only slightly between the methods, and rupture does not occur in all runs performed. Here we computed traveling drops for a ratchet lateral excitation and showed that such an excitation leads to a nonvanishing averaged lateral mean flow of the fluid.

Since primitive variables are used, the algorithm presented in this paper can be extended straightforwardly to three dimensions. However, due to the high computational effort, a parallel computation of the sparse linear system (33) and semi-implicit time marching would be in order.

Three-dimensional phenomena could then be investigated, especially three-wave interactions and the associated quasiperiodic patterns as well as lateral drop manipulation with possible applications to microfluidics. This work is currently in progress.

ACKNOWLEDGMENTS

We thank Alexander Oron and Elad Sterman-Cohen, Technion Haifa, for ongoing and helpful discussions. This work was supported by the German-Israeli Foundation (GIF), Grant No. 1228-405.10.

APPENDIX

The right-hand sides of (31) on the v-grid read for $j = 2 \dots N$

$$\begin{aligned} F^x_{ij} = {} & \frac{u_{ij}}{\Delta t} + \frac{w_{ij}}{h_{i-1/2}}\frac{\partial u_{i,j}}{\partial z} + (j-1)\Delta z(\dot{\xi}_{i-1/2} + \xi'_{i-1/2}u_{ij})\frac{\partial u_{i,j}}{\partial z} \\ & + \frac{\partial^2 u_{i,j}}{\partial x^2} + \frac{1}{2}\left[((j-1)\Delta z\xi'_{i-1/2})^2 + \frac{1}{h^2_{i-1/2}}\right]\frac{\partial^2 u_{i,j}}{\partial z^2} \\ & - 2(j-1)\Delta z\xi'_{i-1/2}\frac{\partial^2 u_{i,j}}{\partial x \partial z} + 2(j-1)\Delta z\left(2\xi'^2_{i-1/2} - \frac{h''_i}{h_{i-1/2}}\right)\frac{\partial u_{i,j}}{\partial z}, \end{aligned} \tag{A1a}$$

$$\begin{aligned} F^z_{ij} = {} & \frac{w_{ij}}{\Delta t} + \frac{w_{ij}}{h_{i-1/2}}\frac{\partial w_{i,j}}{\partial z} + (j-1)\Delta z(\dot{\xi}_{i-1/2} + \xi'_{i-1/2}u_{ij})\frac{\partial w_{i,j}}{\partial z} \\ & + \frac{\partial^2 w_{i,j}}{\partial x^2} + \frac{1}{2}\left[((j-1)\Delta z\xi'_{i-1/2})^2 + \frac{1}{h^2_{i-1/2}}\right]\frac{\partial^2 w_{i,j}}{\partial z^2} \\ & - 2(j-1)\Delta z\xi'_{i-1/2}\frac{\partial^2 w_{i,j}}{\partial x \partial z} + 2(j-1)\Delta z\left(2\xi'^2_{i-1/2} - \frac{h''_i}{h_{i-1/2}}\right)\frac{\partial w_{i,j}}{\partial z}. \end{aligned} \tag{A1b}$$

For $j = 1$ we take

$$F^x_{i,1} = \frac{1}{h^2_{i-1/2}}\frac{u_{i,3} - 2u_{i,2}}{\Delta z^2}, \tag{A2a}$$

$$F^z_{i,1} = \frac{1}{h^2_{i-1/2}}\frac{2w_{i,2}}{\Delta z^2}. \tag{A2b}$$

The derivatives h' and h'' are expressed on the v-grid according to

$$h'_i = \frac{h_i - h_{i-1}}{\Delta x}, \tag{A3a}$$

$$h''_i = \frac{h_{i+1} - h_i - h_{i-1} + h_{i-2}}{2\Delta x^2}. \tag{A3b}$$

Central differences of order Δx, Δz are taken to calculate the first, second, and mixed derivatives of $\vec{v}$ with respect to x and z. At $j = N$ we apply the boundary condition (19):

$$\frac{\partial u_{i,N}}{\partial z} = \frac{h_{i-1/2}}{\left(1 + h'^2_i\right)^2}\left(h'\left(h'^2_i + 3\right)\frac{\partial u_{i,N}}{\partial x} - \left(1 - h'^2_i\right)\frac{\partial w_{i,N}}{\partial x}\right), \tag{A4}$$

and by the help of the continuity equation

$$\frac{\partial w_{i,N}}{\partial z} = h_i' \frac{\partial u_{i,N}}{\partial z} - h_{i-1/2} \frac{\partial u_{i,N}}{\partial x}. \tag{A5}$$

At $j = 1$ we take

$$\frac{\partial^2 u_{i,1}}{\partial z^2} = \frac{u_{i,3} - 2u_{i,2}}{\Delta z^2}, \tag{A6a}$$

$$\frac{\partial^2 w_{i,1}}{\partial z^2} = \frac{2w_{i,2}}{\Delta z^2}. \tag{A6b}$$

The nine coefficients occurring in the sparse system (33) read (p-grid)

$$a_{ij}^1 = \frac{1}{4}\left[\frac{(j-1)(\xi_i - \xi_{i-1}) - 1}{\Delta x^2} + \left(j - \frac{1}{2}\right)\frac{(\xi_{i+1} - \xi_{i-1})[(j-1)(\xi_{i-1} - \xi_i) + 1]}{2\Delta x^2} - \frac{1}{h_i h_{i-1/2} \Delta z^2}\right],$$

$$a_{ij}^2 = \frac{1}{4}\left[\frac{\xi_i - \xi_{i-1} - 2}{\Delta x^2} + \left(j - \frac{1}{2}\right)\frac{(2j-1)(\xi_{i+1} + \xi_{i-1})(\xi_i - \xi_{i-1})}{2\Delta x^2} + \frac{2}{h_i h_{i-1/2} \Delta z^2}\right],$$

$$a_{ij}^3 = -\frac{1}{4}\left[\frac{j(\xi_i - \xi_{i-1}) + 1}{\Delta x^2} + \left(j - \frac{1}{2}\right)\frac{(\xi_{i+1} - \xi_{i-1})[j(\xi_i - \xi_{i-1}) + 1]}{2\Delta x^2} + \frac{1}{h_i h_{i-1/2} \Delta z^2}\right],$$

$$a_{ij}^4 = -\frac{1}{4}\left[\frac{(j-1)(\xi_{i+1} - 2\xi_i + \xi_{i-1}) - 2}{\Delta x^2} + \left(j - \frac{1}{2}\right)\frac{(j-1)(\xi_{i+1} - \xi_{i-1})^2}{2\Delta x^2} + \frac{1}{h_i \Delta z^2}\left(\frac{1}{h_{i+1/2}} + \frac{1}{h_{i-1/2}}\right)\right],$$

$$a_{ij}^5 = -\frac{1}{4}\left[\frac{\xi_{i+1} - 2\xi_i + \xi_{i-1} - 4}{\Delta x^2} - \left(j - \frac{1}{2}\right)\frac{(2j-1)(\xi_{i+1} - \xi_{i-1})^2}{2\Delta x^2} - \frac{2}{h_i \Delta z^2}\left(\frac{1}{h_{i+1/2}} + \frac{1}{h_{i-1/2}}\right)\right],$$

$$a_{ij}^6 = \frac{1}{4}\left[\frac{j(\xi_{i+1} - 2\xi_i + \xi_{i-1}) + 2}{\Delta x^2} - \left(j - \frac{1}{2}\right)\frac{j(\xi_{i+1} - \xi_{i-1})^2}{2\Delta x^2} - \frac{1}{h_i \Delta z^2}\left(\frac{1}{h_{i+1/2}} + \frac{1}{h_{i-1/2}}\right)\right],$$

$$a_{ij}^7 = -\frac{1}{4}\left[\frac{(j-1)(\xi_{i+1} - \xi_i) + 1}{\Delta x^2} + \left(j - \frac{1}{2}\right)\frac{(\xi_{i+1} - \xi_{i-1})[(j-1)(\xi_{i+1} - \xi_i) + 1]}{2\Delta x^2} + \frac{1}{h_i h_{i+1/2} \Delta z^2}\right],$$

$$a_{ij}^8 = -\frac{1}{4}\left[\frac{\xi_{i+1} - \xi_i + 2}{\Delta x^2} - \left(j - \frac{1}{2}\right)\frac{(2j-1)(\xi_{i+1} - \xi_{i-1})(\xi_{i+1} - \xi_i)}{2\Delta x^2} - \frac{2}{h_i h_{i+1/2} \Delta z^2}\right],$$

$$a_{ij}^9 = \frac{1}{4}\left[\frac{j(\xi_{i+1} - \xi_i) - 1}{\Delta x^2} - \left(j - \frac{1}{2}\right)\frac{(\xi_{i+1} - \xi_{i-1})[j(\xi_{i+1} - \xi_i) - 1]}{2\Delta x^2} - \frac{1}{h_i h_{i+1/2} \Delta z^2}\right].$$

[1] M. Faraday, On the forms and states assumed by fluids in contact with vibrating elastic surfaces, Phil. Trans. R. Soc. Lond. **121**, 319 (1831).

[2] T. B. Benjamin and F. Ursell, The stability of the plane free surface of a liquid in vertical periodic motion, Proc. R. Soc. London, Ser. A **225**, 505 (1954).

[3] K. Kumar and L. S. Tuckerman, Parametric instability of the interface between two fluids, J. Fluid Mech. **279**, 49 (1994).

[4] J. Beyer and R. Friedrich, Faraday instability: Linear analysis for viscous fluids, Phys. Rev. E **51**, 1162 (1995).

[5] J. Bechhoefer, V. Ego, S. Manneville, and B. Johnson, An experimental study of the onset of parametrically pumped surface waves in viscous fluids, J. Fluid Mech. **288**, 325 (1995).
[6] C. Wagner, H.-W. Müller, and K. Knorr, Pattern formation at the bicritical point of the Faraday instability, Phys. Rev. E **68**, 066204 (2003).
[7] G. H. Wolf, The dynamic stabilization of the Rayleigh-Taylor instability and the corresponding dynamic equilibrium, Z. Phys. **227**, 291 (1969).
[8] M. Bestehorn and A. Pototsky, Faraday instability and nonlinear pattern formation of a two-layer system: A reduced model, Phys. Rev. Fluids **1**, 063905 (2016).
[9] W. S. Edwards and S. Fauve, Patterns and quasi-patterns in the Faraday experiment, J. Fluid Mech. **278**, 123 (1994).
[10] B. Christiansen, P. Alstrom, and M. T. Levinsen, Ordered Capillary-Wave States: Quasicrystals, Hexagons and Radial Waves, Phys. Rev. Lett. **68**, 2157 (1992).
[11] W. S. Edwards and S. Fauve, Parametrically excited quasicrystalline surface waves, Phys. Rev. E **47**, R788 (1993).
[12] Y. Ding and P. Umbanhowar, Enhanced Faraday pattern stability with three-frequency driving, Phys. Rev. E **73**, 046305 (2006).
[13] C.-S. Yih, Instability of unsteady flows or configurations, J. Fluid Mech. **31**, 737 (1968).
[14] J. Porter, I. Tinao, A. Laveron-Simavilla, and C. A. Lopez, Pattern selection in a horizontally vibrated container, Fluid Dyn. Res. **44**, 065501 (2012).
[15] J. M. Perez-Gracia, J. Porter, F. Varas, and J. M. Vega, Subharmonic capillary-gravity waves in large containers subject to horizontal vibrations, J. Fluid Mech. **739**, 196 (2014).
[16] M. Higuera, J. Porter, F. Varas, and J. M. Vega, Nonlinear dynamics of confined liquid systems with interfaces subject to forced vibrations, Adv. Colloid Interface Sci. **206**, 106 (2014).
[17] F. Varas and J. M. Vega, Modulated surface waves in large-aspect-ratio horizontally vibrated containers, J. Fluid Mech. **579**, 271 (2007).
[18] D. Bensimon, P. Kolodner, C. M. Surko, H. Williams, and V. Croquette, Competing and coexisting dynamical states of travelling-wave convection in an annulus, J. Fluid Mech. **217**, 441 (1990).
[19] I. D. Borcia, R. Borcia, W. Xu, M. Bestehorn, and S. U. Harlander, Tidal bores in a large circular channel, Eur. J. Mech. B (to be published).
[20] H. N. Yoshikawa and J. E. Wesfreid, Oscillatory Kelvin-Helmholtz instability. Part 2. An experiment in fluids with large viscosity contrast, J. Fluid Mech. **675**, 249 (2011).
[21] H. N. Yoshikawa and J. E. Wesfreid, Oscillatory Kelvin-Helmholtz instability. Part 1. A viscous theory, J. Fluid Mech. **675**, 223 (2011).
[22] Y. Gaponenko and V. Shevtsova, Shape of diffusive interface under periodic excitations at different gravity level, Microgravity Sci. Technol. **28**, 431 (2016).
[23] Y. A. Gaponenko, M. Torregrosa, V. Yasnou, A. Mialdun, and V. Shevtsova, Dynamics of the interface between miscible liquids subjected to horizontal vibration, J. Fluid Mech. **784**, 342 (2015).
[24] D. V. Lyubimov and A. A. Cherepanov, Development of a steady relief at the interface of fluids in a vibrational field, Fluid Dyn. **21**, 849 (1986).
[25] A. A. Ivanova, V. G. Kozlov, and P. Evesque, Interface dynamics of immiscible fluids under horizontal vibration, Fluid Dyn. **36**, 362 (2001).
[26] T. P. Lyubimova, The interaction of thermocapillary and vibrational instabilities in a two-layer system subjected to the tangential vibrations, Eur. Phys. J. Spec. Top. **226**, 1263 (2017).
[27] E. Talib and A. Juel, Instability of a viscous interface under horizontal oscillation, Phys. Fluids **19**, 092102 (2007).
[28] E. Talib and S. V. Jalikop, The influence of viscosity on the frozen wave instability: Theory and experiment, J. Fluid Mech. **584**, 45 (2007).
[29] R. V. Craster and O. K. Matar, Dynamics and stability of thin liquid films, Rev. Mod. Phys. **81**, 1131 (2009).
[30] C. Ruyer-Quil and P. Manneville, Improved modeling of flows down inclined planes, Eur. Phys. J. B **15**, 357 (2000).

[31] N. O. Rojas, M. Argentina, E. Cerda, and E. Tirapegui, Inertial Lubrication Theory, Phys. Rev. Lett. **104**, 187801 (2010).
[32] M. Bestehorn, Q. Han, and A. Oron, Nonlinear pattern formation in thin liquid films under external vibrations, Phys. Rev. E **88**, 023025 (2013).
[33] M. Bestehorn, Laterally extended thin liquid films with inertia under external vibrations, Phys. Fluids **25**, 114106 (2013).
[34] A. Oron, S. H. Davis, and S. G. Bankoff, Long-scale evolution of thin liquid films, Rev. Mod. Phys. **69**, 931 (1997).
[35] A. Pototsky and M. Bestehorn, Faraday instability of a two-layer liquid film with a free upper surface, Phys. Rev. Fluids **1**, 023901 (2016).
[36] S. Richter and M. Bestehorn, Thin-film Faraday patterns in three dimensions, Eur. Phys. J. Spec. Top. **226**, 1253 (2017).
[37] P. Chen and K.-A. Wu, Subcritical Bifurcations and Nonlinear Balloons in Faraday Waves, Phys. Rev. Lett. **85**, 3813 (2000).
[38] P. Chen, Nonlinear wave dynamics in Faraday instabilities, Phys. Rev. E **65**, 036308 (2002).
[39] S. Ubal, M. D. Giavedoni, and F. A. Saita, A numerical analysis of the influence of the liquid depth on two-dimensional Faraday waves, Phys. Fluids **15**, 3099 (2003).
[40] M. Bestehorn and P. A. Tyvand, Merging and colliding bores, Phys. Fluids **21**, 042107 (2009).
[41] J. W. Demmel, S. C. Eisenstat, J. R. Gilbert, X. S. Li, and J. W. H. Liu, A supernodal approach to sparse partial pivoting, SIAM J. Matrix Anal. Appl. **20**, 720 (1999).
[42] E. Sterman-Cohen, M. Bestehorn, and A. Oron, Ratchet flow of thin films induced by a two-frequency tangential forcing, Phys. Fluids **30**, 022101 (2018).